Anthropogenic and Natural Contributions to the Lengthening of the Southern Hemisphere Summer Season

EVAN WELLER,[a] BO-JOUNG PARK,[b] AND SEUNG-KI MIN[b]

[a] *School of Environment, University of Auckland, Auckland, New Zealand*
[b] *Division of Environmental Science and Engineering, Pohang University of Science and Technology, Pohang, South Korea*

(Manuscript received 6 February 2020, in final form 19 July 2020)

ABSTRACT: This study provides the first quantitative assessment of observed long-term changes in summer-season timing and length in the Southern Hemisphere (SH) and its subregions over the past 60 years, enabling a global completeness by complementing such characteristics previously reported for the Northern Hemisphere (NH). Using an objective algorithm that is based on temperature indices, relative measures of summer onset, withdrawal, and duration are determined at each land location over the period 1953–2012. Significant widespread summer-season lengthening, due to earlier onset and delayed withdrawal, has occurred across the SH, a longer period for extreme heat-wave events and wildfires to potentially occur. The asymmetric magnitude (onset vs withdrawal) in summer-season lengthening is slightly less over the SH than over the NH. Contributions of anthropogenic and natural factors to the observed trends in summer-season characteristics were investigated using phase 5 of the Coupled Model Intercomparison Project (CMIP5) multimodel simulations integrated with observed external forcings [anthropogenic plus natural (ALL)], greenhouse gas forcing only (GHG), and natural forcing only [solar and volcanic activities (NAT)]. Overall, consistent with the NH, increased greenhouse gases were the main cause of observed changes in the SH, with negligible contribution from other external forcings. ALL and GHG simulations also reproduced a slight tendency for earlier summer onset to contribute more to summer lengthening. Proportions of observed regional trends in summer-season indices attributable to trends in long-term internal variability in the SH, namely, the interdecadal Pacific oscillation (IPO) and southern annular mode (SAM), suggests such variability can only explain up to ~12%, supporting the dominant role of greenhouse gas forcing.

KEYWORDS: Summer/warm season; Southern Hemisphere; Anthropogenic effects; Climate change; Seasonal variability; Climate models

1. Introduction

As the warmest season of the year, the heat in summer also often translates to drier temperatures in many land regions outside of the tropics. This hot, dry time of year places pressure on water demands because of the increased likelihood or intensification of droughts (Lehmann et al. 2018; AghaKouchak et al. 2014; Kong et al. 2020), and when humans and ecosystems experience heat waves, one of the deadliest forms of extreme weather events worldwide (e.g., Mora et al. 2017). Overall, summer imposes compounded and increased harm to both humans and the environment (Zscheischler and Seneviratne 2017; Pfleiderer et al. 2019). For example, about 30% of the world is already exposed to heat that is intense enough to kill people for 20 or more days each year (Mora et al. 2017). Recent observations suggest that the frequency, duration, and intensity of summer heat-wave events are further increasing over land regions across the globe (e.g., Coumou and Rahmstorf 2012; Cowan et al. 2014; Pfleiderer et al. 2019). Despite various limitations in simulating regional changes (Hao et al. 2013), climate models project these trends to continue with increasing anthropogenic forcing (Meehl and Tebaldi 2004; Coumou and Robinson 2013). Therefore, any change in the seasonal cycle that alters the summer season, such as a lengthening of the summer season (e.g., Peña-Oritz et al. 2015; Park et al. 2018), will simply provide a larger window for these extreme summer heat-wave events to develop and occur. Changes to the seasonal cycle driven by climate change will have large socioeconomic and ecological impacts (Bertram et al. 2001; Christidis et al. 2007; Mueller et al. 2015). A lengthening of the summer season is likely to lead to further increases in the risk of situations that place growing pressure on water demands with an increasing world population and prolong or intensify droughts conditions. Increase in either duration or intensity of drought conditions may also drive increase in the risk of conditions that are associated with widespread wildfire events (Jolly et al. 2015; Abatzoglou et al. 2019), which have had devastating impacts in many regions during recent years, such as the United States (e.g., Williams et al. 2019) and Australia (e.g., Dowdy 2018).

In recent years, global heat records are increasingly being broken as a result of anthropogenic forcing (Coumou et al. 2013; Pfleiderer et al. 2019). The link between global climate change, due to increasing greenhouse gases, and the increase in temperature and/or heat waves is well established (IPCC 2013, and references therein). Observed phase and amplitude changes over recent decades in the seasonal cycle are well documented to be a result from both external forcings and large-scale atmospheric variability (e.g., Mann and Park 1996;

Supplemental information related to this paper is available at the Journals Online website: https://doi.org/10.1175/ JCLI-D-20-0084.s1.

Corresponding author: Evan Weller, evan.weller@auckland.ac.nz

DOI: 10.1175/JCLI-D-20-0084.1

Wallace and Osborn 2002; Stine et al. 2009; Dwyer et al. 2012; Qian and Zhang 2015; Cornes et al. 2017). Yet there are still knowledge gaps in terms of the impact of such forcing on different characteristics of the ''meteorological'' seasons (i.e., the 12 months of the year being divided up into four seasons with 3 months each). In particular, the contributions from anthropogenic and natural forcings to observed long-term variations in summer-season timing and length over global land areas remain unclear.

Building on the attribution of several regional changes in growing- and/or summer-season length and timing to anthropogenic forcing (e.g., Christidis et al. 2007; Stine et al. 2009; Qian et al. 2012; Mueller et al. 2015; Peña-Oritz et al. 2015), Park et al. (2018) recently examined the timing and length of the summer season over the entire Northern Hemisphere (NH) land areas. Similar to studies that quantified changes in the seasonal cycle by seasonal indicators or through threshold crossing statistics, Park et al. (2018) undertook an objective analysis using temperature-based indices (devised from previous studies of growing-season length) to determine relative measures of summer onset, withdrawal, and duration at each NH land location. Overall, the observations for the past 60 years (1953–2012) show lengthening of the summer season as a result of both an earlier onset and delayed withdrawal of summer across the NH. Further, the summer onset advance contributed more to the observed increase in summer-season length in many regions than the delay of summer withdrawal, possibly linked to changes in the phase of the seasonal cycle (e.g., Stine et al. 2009; Dwyer et al. 2012) and the influence of internal climate variability (e.g., Christidis et al. 2007; Stine and Huybers 2012). Subsequently, it was found that increased greenhouse gases were the main cause of the observed changes and multidecadal variability explained no more than 10% of the observed trends in summer-season length, mainly over the high latitudes. To date, such information is lacking for Southern Hemisphere (SH) land areas.

To complete a global examination of the observed long-term variations in summer-season timing and length, we build on Park et al. (2018) who previously reported on such characteristics for the NH. Here, we have conducted a complementary systematic analysis of similar long-term variations in summer-season timing and length over land of the SH and its subregions during the past 60 years (1953–2012). Using a revised objective algorithm based on temperature indices, we determine the relative measures of summer onset, withdrawal, and duration at each land location. Following this, contributions of anthropogenic and natural factors to the observed trends in summer-season characteristics were investigated through comparisons with multimodel simulations integrated with different external forcings. Overall, this study enables a global completeness by providing the first quantitative assessment of the observed changes in summer-season length in the SH. The remainder of the paper is structured as follows. Section 2 describes the data and the method used to obtain summer-season characteristics based on an objective algorithm. In section 3, the long-term variations in summer-season timing and length over land of the SH and its subregions and the contributions of anthropogenic and natural factors to the observed trends in summer-season characteristics are examined. Section 4 contains a summary and conclusions.

2. Data and methods

a. Observations and model data

Gridded observations of daily temperatures over the SH land were obtained from the Berkeley Earth project (http://berkeleyearth.org/data/; Rohde et al. 2013) dataset for the period of 1953–2012. Daily mean temperatures were provided with a resolution of 1° longitude × 1° latitude and are constructed utilizing over 39 000 unique stations, which provides increased coverage of land areas in the SH relative to other datasets that are available [e.g., Hadley Centre's Global Historical Climatology Network Daily (HadGHCND) dataset (Caesar et al. 2006)] with reduced uncertainty (Rohde et al. 2013). In addition, consistent with Park et al. (2018), we limit the analysis domain to extratropical areas where a distinct annual cycle occurs (cf. Christidis et al. 2007) and also exclude Antarctica. Therefore, the overall analysis domain covers the land regions over 23.5°–60°S. Note that, for all maps in the results, the land size for New Zealand has been magnified by a factor of 2 to aid in the visualization, and the maps show original values (i.e., values are not multiplied by a factor of 2).

Daily mean historical temperature simulations were obtained from the multimodel dataset of phase 5 of the Coupled Model Intercomparison Project (CMIP5) experiments (Taylor et al. 2012), which were carried out under the observed external forcings. A list of the model simulations used in this study is provided in Table 1. Overall, three experiments available for the analysis period were used to compare with the observed results: 1) anthropogenic (greenhouse gases and aerosols emissions) plus natural (solar plus volcanic activities) forcing runs (ALL; 24 models) constructed by merging historical simulations (1953–2005) with future projections based on the representative concentration pathway 4.5 (RCP4.5) scenario (2006–12); 2) greenhouse gas–only forcing (GHG; 6 models); and 3) natural-only forcing (NAT; 8 models). For the GHG and NAT simulations, the period 1952–2011 was used due to the end date of the individual forcing simulations yet has no influence on the overall trends for the analysis period.

All model data (summer-season indices; see below) were interpolated to the same resolution as the observations (OBS) using a bilinear interpolation method (''remapbil'' algorithm from the Climate Data Operators; https://code.zmaw.de/projects/cdo/embedded/index.html) with the same land–sea mask being applied. Note that models have differing land–sea masks from the observations, particularly along the coast and in coarser models. Sensitivity tests found that the use of each model's land mask did not affect the main results based on regional averages (not shown).

b. Summer-season indices

Summer-season indices in the SH were defined based on a relative threshold that is applied for each grid, following the method of Park et al. (2018) in the NH. To reduce the influence of day-to-day temperature fluctuations, the daily temperature

TABLE 1. List of CMIP5 models and experiments. Number of ensemble members for each model is shown for ALL, GHG, and NAT experiments and the total number of models is shown for each experiment. Expansions for model acronyms are available online (https://www.ametsoc.org/PubsAcronymList).

	Model	ALL	GHG	NAT
1	ACCESS1.0	1	—	—
2	ACCESS1.3	1	3	3
3	BCC_CSM-1.1(m)	1	—	—
4	BNU-ESM	1	—	—
5	CanESM2	3	5	5
6	CCSM4	3	—	—
7	CNRM-CM5	1	5	6
8	CSIRO Mk3.6.0	9	10	10
9	EC-EARTH	1	—	—
10	GFDL CM3	2	—	—
11	GISS-E2-R	1	—	—
12	HadCM3	9	—	—
13	HadGEM2-AO	1	—	—
14	HadGEM2-ES	2	4	4
15	INM-CM4.0	1	—	—
16	IPSL-CM5A-LR	3	4	3
17	IPSL-CM5A-MR	1	—	3
18	MIROC4h	2	—	—
19	MIROC5	3	—	—
20	MIROC-ESM	1	—	—
21	MPI-ESM-LR	3	—	—
22	MPI-ESM-MR	3	—	—
23	MRI-CGCM3	1	—	–
24	NorESM1-M	1	—	1
Total	Model (runs)	24 (55)	6 (31)	8 (35)

data were first smoothed. However, here we apply a fourth-harmonic function as opposed to a third-degree polynomial for each grid box where no data were missing for the given year (Fig. 1a). The equation for the fourth-harmonic fit $\tilde{T}(t)$ can be expressed as

$$\tilde{T}(t) = T_0 + \sum_{k=1}^{4} [A_k \cos(\omega_k t) + B_k \sin(\omega_k t)], \qquad (1)$$

where t indicates day of the year ($t = 1, \ldots, 365$), k is the number of the harmonic, and $\omega_k = 2\pi k/365$; T_0 depicts annual mean of the given year, and coefficients A_k and B_k are obtained from a Fourier transform. The choice to use a fourth-harmonic function is due to it providing a better fit to the overall daily seasonal cycle with less root-mean-square error (RMSE), that is, better representing interseasonal fluctuations than a third-degree polynomial fit. Overall, the harmonic smoothing performed best at eliminating smaller-time-scale noise, and trends in the indices were robust to the smoothing method chosen, suggesting any influence from spurious oscillations (e.g., Gibbs oscillations) to be negligible.

The local gridpoint temperature threshold for the summer season was simply defined as the 75th percentile of temperature values averaged over 1953–2012 (i.e., the warmest quarters of the year) (Trenberth 1983). An example of this local threshold for one location is provided in Fig. 1a (red horizontal line) and the spatial distribution of local temperature thresholds for SH land areas is shown in Fig. 1b. Similar to the NH, there is a general dependency on latitudes, as highlighted by the latitudinal profile of the zonal mean (right panel in Fig. 1b), with thresholds increasing toward lower latitudes. However, the influence of altitude is also evident over some continents (e.g., the west coast of South America). Summer onset is defined as the calendar date when the smoothed temperature curve begins to exceed the local temperature threshold, and summer withdrawal is defined as the date when the temperature decreases below that threshold. Summer duration is defined simply as the number of days from summer onset to summer withdrawal (Fig. 1a). Hereinafter, summer onset (ONS), withdrawal (WIT), and duration (DUR) are referred to as "summer-season indices."

Overall, sensitivity tests conducted in terms of the use of different local thresholds criteria or datasets found that results do not change significantly. For example, Park et al. (2018) tested comparisons of the summer-season indices obtained from either different percentile thresholds (e.g., 70th or 80th percentile) or an absolute threshold of a daily maximum temperature [e.g., Klein Tank and Können (2003)]. Here, the fourth-harmonic function fitting was also compared with those obtained from the third-degree polynomial fitting previously used for the NH by Park et al. (2018) (cf. Figs. 1a and 1c). In addition, thresholds and trends in the SH summer-season indices were calculated using the HadGHCND dataset, which, however, provide less coverage in the SH. Note, some local thresholds (Figs. 1a,c) and/or individual summer-season dates (i.e., a maximum difference of ±2 days, not shown) were found to be slightly different across the two filtering methods or datasets. Nevertheless, both the spatial patterns of the climatology and the trends of summer-season indices were largely similar between the following results, as were the results from using different thresholds and filtering methods or dataset, indicating the robustness of the applied methods used. However, asymmetry in contributions from summer onset and withdrawal to the overall summer-season lengthening was found to be slightly sensitive to the smoothing method and will be discussed later.

c. *Attribution analysis*

To identify causes of the observed changes in summer-season indices, we estimated contributions of external forcing and natural large-scale multidecadal variability to the observed trends in the SH and its subregions. Long-term natural variability of the ocean such as the interdecadal Pacific oscillation (IPO) has been shown to affect decadal variability of land temperatures (e.g., Salinger et al. 2001; Meehl et al. 2012). Here, the IPO index was obtained from the National Oceanic and Atmospheric Administration (NOAA) Earth System Research Laboratory (ESRL), and is based on the difference between the sea surface temperature anomalies averaged over the central equatorial Pacific and the average in the northwest and southwest Pacific (Henley et al. 2015). Defining the IPO using the tripole index accounts for variability in the South Pacific, often not considered using other indices based on principal component analysis over the North Pacific. Overall,

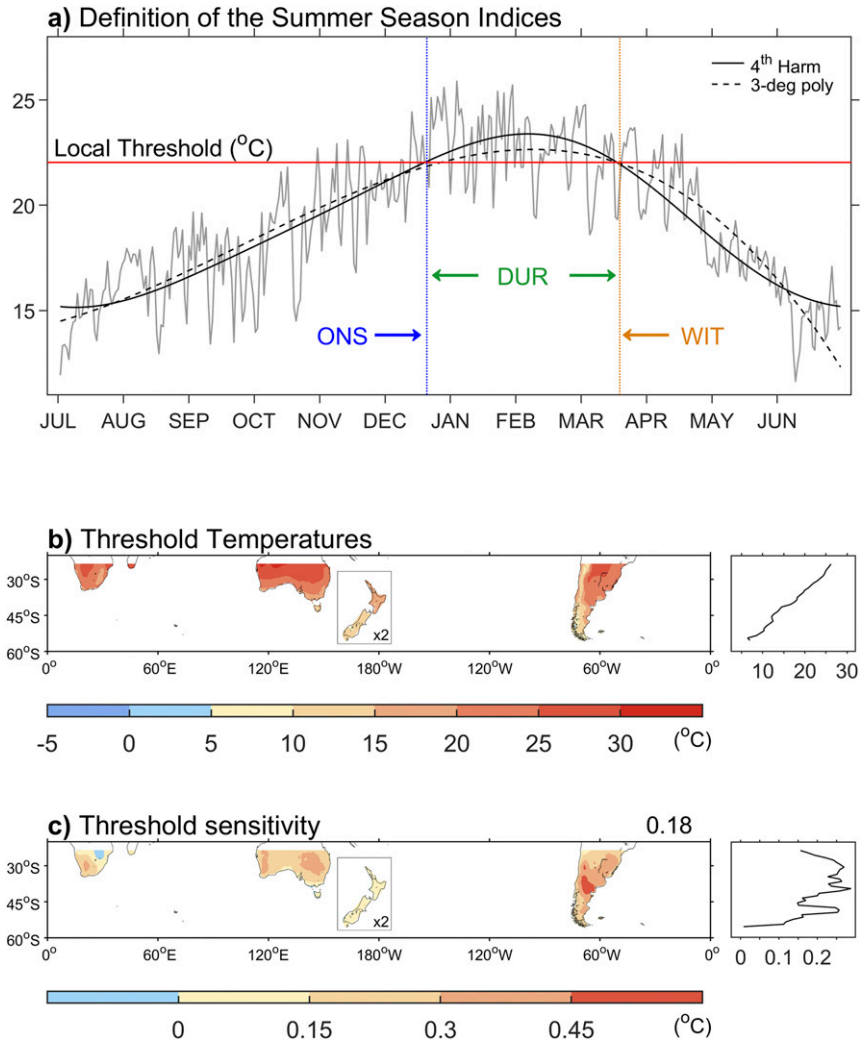

FIG. 1. (a) Example of the definitions of the summer-season indices (onset, withdrawal, and duration). The horizontal red line indicates the local temperature threshold (75th percentile). Also shown is the comparison of fit to daily temperatures using a fourth harmonic (solid) and third-degree polynomial (dashed) curve. (b) The spatial distribution of local temperature thresholds across the Southern Hemisphere using a fourth harmonic curve fit. (c) The difference (fourth harmonic minus third-degree polynomial) between thresholds as calculated using the two curve fits. Zonal mean distributions are displayed to the right in (b) and (c).

the IPO tripole index time series bears a close resemblance (i.e., correlations >0.92) to previously published PC-based indices (Henley et al. 2015). A small but positive trend in the IPO for the 60 years is observed (over a negative–positive–negative phase transition during the period), therefore, potentially contributing to the observed trend in summer-season indices. The southern annular mode (SAM) is associated more with influencing interannual variability of land temperatures (e.g., Hendon et al. 2007; Min et al. 2013; Harris and Lucas 2019), yet an overall positive trend in the SAM index has also been observed over recent decades (Clem et al. 2020). Therefore, SAM contributions to the observed trend in summer-season indices were also assessed using the difference in normalized zonal-mean sea level pressure between 40° and 65°S (Gong and Wang 1999). Note, the positive SAM trend is also predominantly attributed to external forcing such as greenhouse gas increases and stratospheric ozone losses (e.g., Arblaster and Meehl 2006; Gerber and Son 2014). Other modes of variability, such as the Atlantic multidecadal oscillation and El Niño–Southern Oscillation (ENSO), did not contribute to any trends in the observed summer-season indices and therefore not presented. All monthly indices were averaged over each summer season [December–March (DJFM)].

Following Park et al. (2018), we employed a stepwise regression method to determine the relative contributions of external forcing and multidecadal climate variability on the

three summer-season indices over the whole SH and its subregions. Overall, this involved calculating the proportion of the observed trend attributable to external (ALL, including anthropogenic plus natural) forcing. First, the following equation is calculated:

$$Y_{\mathrm{OBS}} = \beta_1 X_{\mathrm{ALL}} + \varepsilon, \tag{2}$$

where Y_{OBS} is the observed area-averaged time series of the summer-season index, X_{ALL} is the multimodel mean (ALL forcing runs) of the area-averaged time series of the summer-season index, β_1 is the regression coefficient, and ε is the residual. The residual ε represents the observed changes without external forcing, or simply the internal variability. Subsequently, a simple linear regression onto the climate variability index (IPO or SAM index) was then taken to estimate its contribution to the residual such that

$$\varepsilon = \beta_2 X_{\mathrm{index}} + \upsilon, \tag{3}$$

where X_{index} represents either the observed IPO or SAM index, β_2 is the regression coefficient, and the residual of this equation is denoted by υ.

The proportion of the observed trend attributable to ALL forcing (P1) was estimated by dividing the linear trend of the ALL regressed term [$\Delta(\beta_1 X_{\mathrm{ALL}})$] by the linear trend of the observed summer-season indices (ΔY_{OBS}):

$$\mathrm{P1} = \Delta(\beta_1 X_{\mathrm{ALL}})/\Delta Y_{\mathrm{OBS}}. \tag{4}$$

Similarly, the proportion of the trend attributable to the climate variability index X_{index} (P2) was calculated as

$$\mathrm{P2} = \Delta(\beta_2 X_{\mathrm{index}})/\Delta Y_{\mathrm{OBS}}. \tag{5}$$

For example, if the IPO index is selected as X_{index}, the trend attributable to IPO can be obtained. This method was also applied to the SAM index. Here, we only assessed linear responses and do not consider nonlinear responses in summer-season indices.

The significance of the estimated contributions of ALL forcing and IPO or SAM to the observed trends was assessed by utilizing each model run (ALL forcing runs) as pseudo observations because each model run, not multimodel mean, is comparable to the observations as a single realization (Paik et al. 2017). For each pseudo observation, we estimated the contributions of ALL and IPO/SAM in the same way as we did for the observations. More specifically, we repeated the procedure from Eq. (2) to Eq. (5) using each ALL forcing run and estimated trends attributable to ALL forcing (P1) and to each type of the simulated multidecadal climate variability (P2). Here the only difference is that multimodel mean for ALL runs is calculated excluding the selected run and that the IPO or SAM index defined from the selected run is used. After repeating this calculation across all model runs, we then assessed the 5%–95% uncertainty ranges of P1 and P2. This way of estimating uncertainty ranges is fundamentally identical to those employed in formal detection and attribution methods (e.g., Allen and Stott 2003). Previous studies have shown that the CMIP5 models simulate reasonably well spatial and temporal characteristics of the IPO (Meehl et al. 2016; Henley et al. 2017) and the SAM (Gillett and Fyfe 2013; Swart et al. 2015).

3. Results

a. Observed summer-season changes

Figure 2 shows the spatial patterns of observed climatological means for the summer indices over the SH. There is an evident contrast of later onset (e.g., mid-to-late December) and withdrawal (e.g., mid-to-late March) in summer at the coast compared to earlier summer beginning (e.g., late November) and end (e.g., late February to early March) farther inland on each continent, or more northern regions. Presumably due to the latitude, size, and island nature of New Zealand, coastal-inland contrast in summer-season indices is weaker compared to the other landmasses, with the most delayed onset and withdrawal on average. However, the duration for each landmass remained somewhat consistent. On average, summer started on 7 December and ended on 6 March, lasting ~90 days in total. The overall range in the summer duration over the SH is about 1.5 weeks (i.e., ranging from 85 to 96 days).

The spatial distribution of the respective trend patterns in the three summer-season indices over the period 1953–2012 is presented in Fig. 3. Areas filled with hatching denote where a local trend is not significant (at the 5% level). Over the 60-yr period, summer onset now begins on average about two weeks earlier (15 days) and summer withdrawal occurs about two weeks later (13 days). Consequently, this has seen the duration of summer increase by almost one month on average (28 days). However, spatial variations reveal several notable differences. Southern Africa and southern America experience larger trends in earlier summer onset over more northern regions, whereas the larger trends occur over the southern regions of Australia. Interestingly, the two islands of New Zealand are found to have opposite trends in not only onset, but all three summer-season indices, yet note that trends are only significant mostly in the far north and far south of the North and South Islands, respectively. For example, in New Zealand summer begins about 14 day earlier on the northern island (situated roughly ~34°–41°S) but begins about 7 days later on the southern island (situated roughly ~40°–47°S). Similarly, the summer season ends later on the northern island and earlier on the southern island of New Zealand, respectively (Fig. 3b). The remainder of the landmasses show clear delays in summer withdrawal, except for parts of Western Australia, where a small region of significant earlier summer withdrawal is found (Fig. 3b).

Overall, the largest extensions in the duration of the SH summer season (Fig. 3c) are apparent over the western and northern regions of southern Africa, central-to-eastern Australia, and northern regions of southern America. Again, New Zealand experiences oppositely signed trends in summer duration, extending in the north and decreasing in the south, most of which are not significant. Domain-averaged trends were also calculated over the four main landmass regions in the SH (Fig. 4a) to further assess contributions from the regional

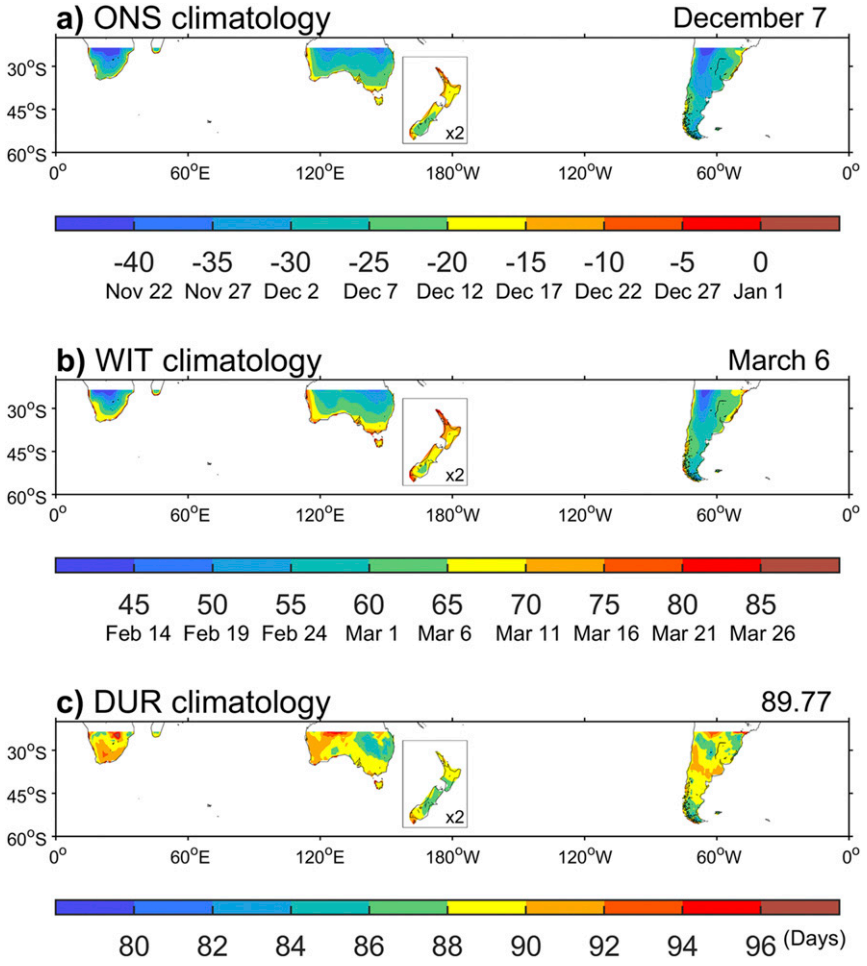

FIG. 2. The spatial patterns of the observed climatology (1953–2012 averages) for (a) summer onset, (b) summer withdrawal, and (c) summer duration. Area means are given in the top-right corner of (a)–(c).

trends in onset and withdrawal to the regional lengthening trends over the period 1953–2012 (Fig. 4b). The domain-averaged trends of all three summer-season indices are largest over the southern Africa region, with a lengthening in summer of about 47 days $(60\,\mathrm{yr})^{-1}$. Understandably, New Zealand shows the weakest mean trends, about 4 days $(60\,\mathrm{yr})^{-1}$, due to oppositely signed trends of the two islands. Similarly, trends in southern America summer-season indices, including lengthening, are stronger than that for Australia because of small regions of oppositely signed trends over Australia (Fig. 3). Further, larger contributions from either the summer onset trend or summer withdrawal trend are not as apparent in the SH, implying that summer duration was extended only marginally more by an earlier start (contributing ~54% to the extension) than a delayed ending. This is in contrast to the NH, where all regions exhibit a stronger summer onset trend than the withdrawal trend, hence summer duration was extended more so by the earlier start (contributing ~60% to the extension) than by the delayed ending to summer. Additional tests found that the asymmetry in summer-season lengthening was sensitive to the smoothing method used to initially fit the daily temperature data. For example, earlier onset trends in the NH (calculated using a third-degree polynomial fit) became slightly weaker when applying a fourth harmonic fit, explaining a similar ~54% of the duration trend in both hemispheres. Additionally, the onset contribution in the SH increases to ~57% when applying a third-degree polynomial fit. Therefore, ONS contributes 54%–57% to the summer lengthening in the SH. Larger land–sea ratio in the NH seems to be related to its stronger sensitivity of summer-season lengthening to the smoothing methods than in the SH, which warrants further investigation.

To assess possible links between observed long-term changes and variability in the summer-season temperature with the summer-season indices, we calculated the relationship between summer-season duration and observed temperatures during the SH summer period (Fig. 5). Over the 60-yr period 1953–2012, in line with global warming, all of the regions that exhibit significant summer [December–February (DJF)] temperature trends in the SH show warming of $>0.28°\mathrm{C}\ (60\,\mathrm{yr})^{-1}$

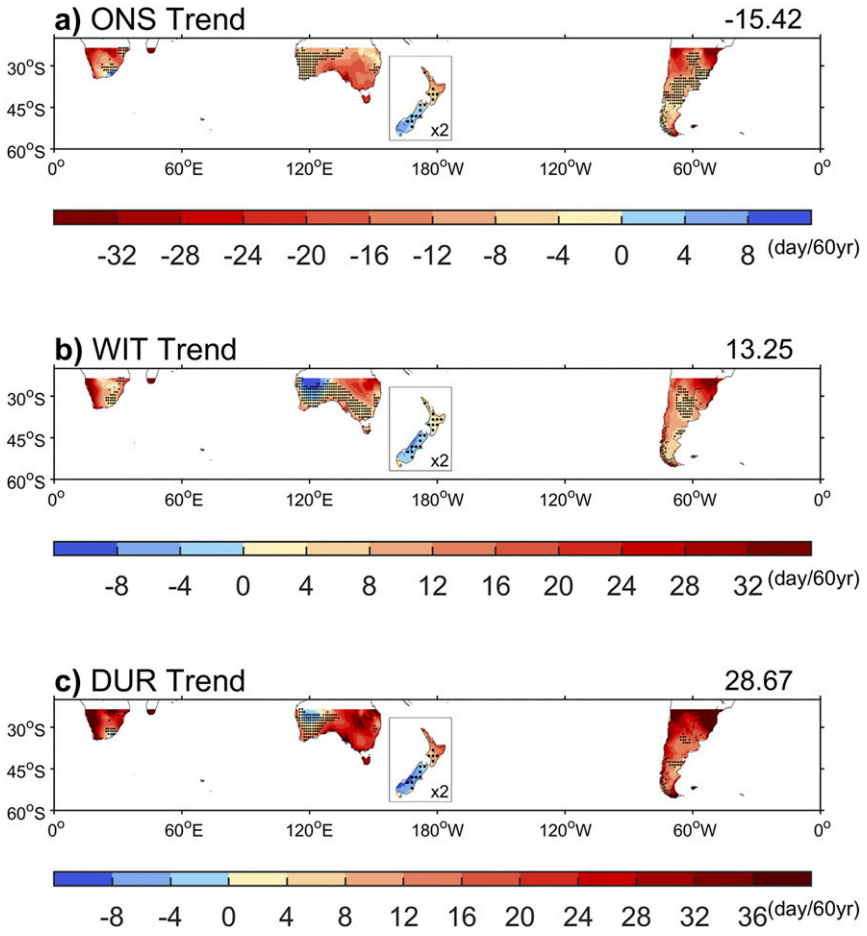

FIG. 3. The spatial distribution of the observed trends over 1953–2012 for (a) summer onset, (b) summer withdrawal, and (c) summer duration. Hatching indicates grids that are not statistically significant trends at the 5% level. Area means are given in the top-right corner of (a)–(c).

(Fig. 5a), with a pattern similar to those for the summer-season indices (Fig. 3), except for where summer duration decreased. Regions that do exhibit a decrease in summer duration (e.g., Western Australia and southern New Zealand), however, show warming trends that are relatively weak and/or not significant (cf. Fig. 3c and Fig. 5a). In the NH, regions where summer duration has decreased (e.g., part of the eastern United States) also coincided with weak negative trends in the summer temperature (see Fig. 5a of Park et al. 2018). Overall, the interannual variability of the summer-season indices were found to be highly correlated with DJF mean temperatures at the local scale (Fig. 5b), and to a lesser extent the long-term change. For example, the temporal correlation between the summer duration and DJF mean temperatures was strong over the majority of the SH land regions (area mean of 0.71), yet there was no distinct relationship with latitude, coastal-inland, or magnitude of the DJF temperature change. Minimal change in correlations was found when the temporal correlation was calculated using detrended data (Fig. 5b, bottom panel). This suggests that the long-term trend in DJF temperatures contributed little to the temporal correlation and the results are not simply because summer-season thresholds are exceeded more easily because temperatures have increased. Interestingly, summer-season indices in New Zealand were found to be widely correlated with temperature changes (>0.69), with no difference between the two islands, such as was evident in the trend of summer-season indices.

b. Simulated summer-season changes in CMIP5

To understand the influences of external forcing factors on the observed summer-season indices over the past 60 years, we employ the multimodel dataset of CMIP5 and their ALL, GHG, and NAT forcing simulations (Table 1) as discussed in section 2. The ALL forcing simulation, which incorporates anthropogenic (greenhouse gases and aerosols emissions) plus natural (solar plus volcanic activities) forcing represents well the overall mean climatological patterns of the observed summer-season onset and withdrawal (cf. Fig. 6 and Fig. 2). Spatial patterns of the individual CMIP5 models' bias for summer onset and withdrawal are provided in Fig. S1 in the

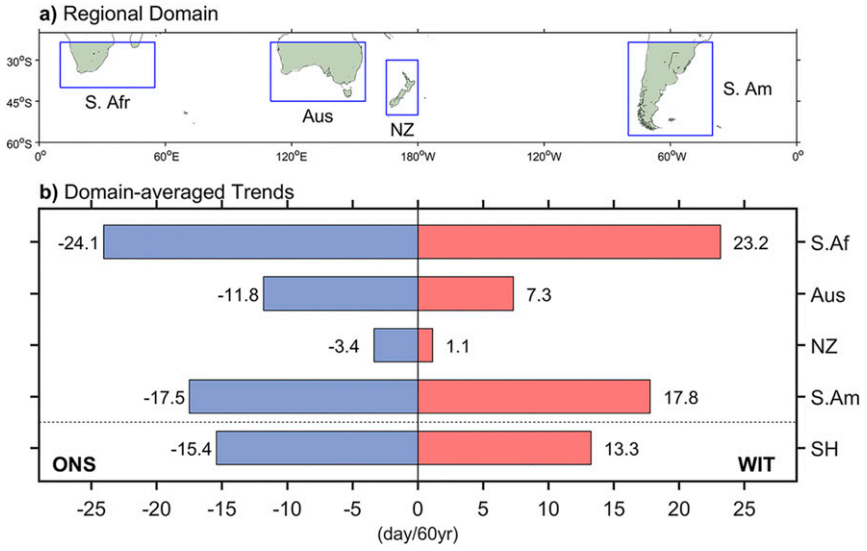

FIG. 4. (a) The SH regional domains used in this study and abbreviations for the corresponding regions, and (b) regional trends of summer onset (blue bars), withdrawal (red bars), and duration (sum of blue and red bars).

online supplemental material. The models represent the two key features of the observations, being that of later onset and withdrawal in summer at the coast as compared with farther inland, and overall delayed responses across of all New Zealand compared to the other landmasses. Interestingly, this oceanic thermal capacity that leads to the coastal-inland contrast is found to be stronger in the models than in the observations. This is opposite to that found in the NH where the

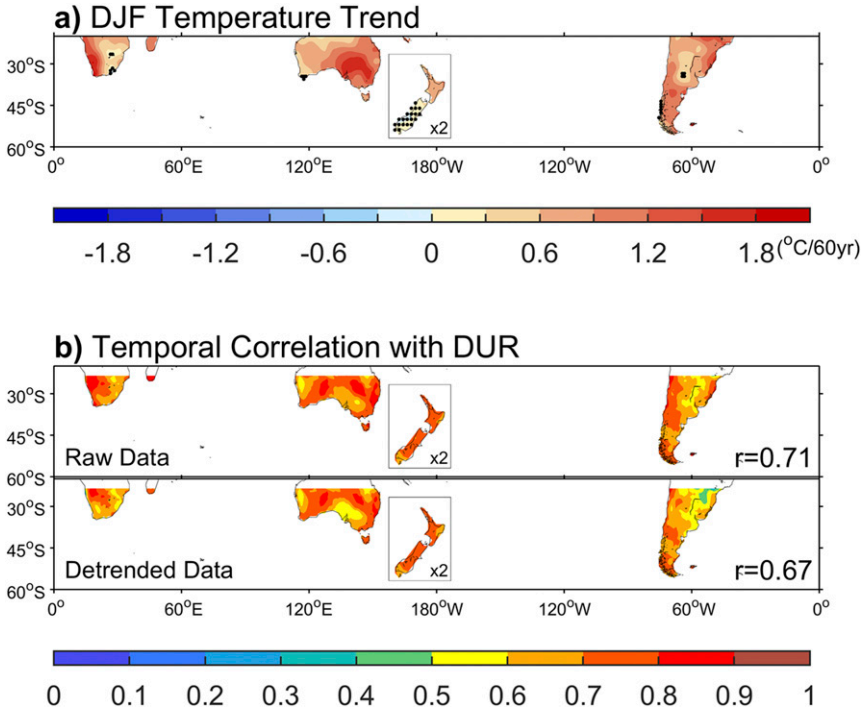

FIG. 5. (a) Spatial pattern of the observed trends in summer mean (DJF) temperatures. Hatching indicates grids with trends that are not statistically significant (at the 5% level). (b) Spatial patterns of the temporal correlation coefficients between the raw (top half of panel) and detrended (bottom half of panel) DJF temperature and the summer duration index (DUR) over 1953–2012. Area mean correlations are given in the bottom-right corner of each half panel.

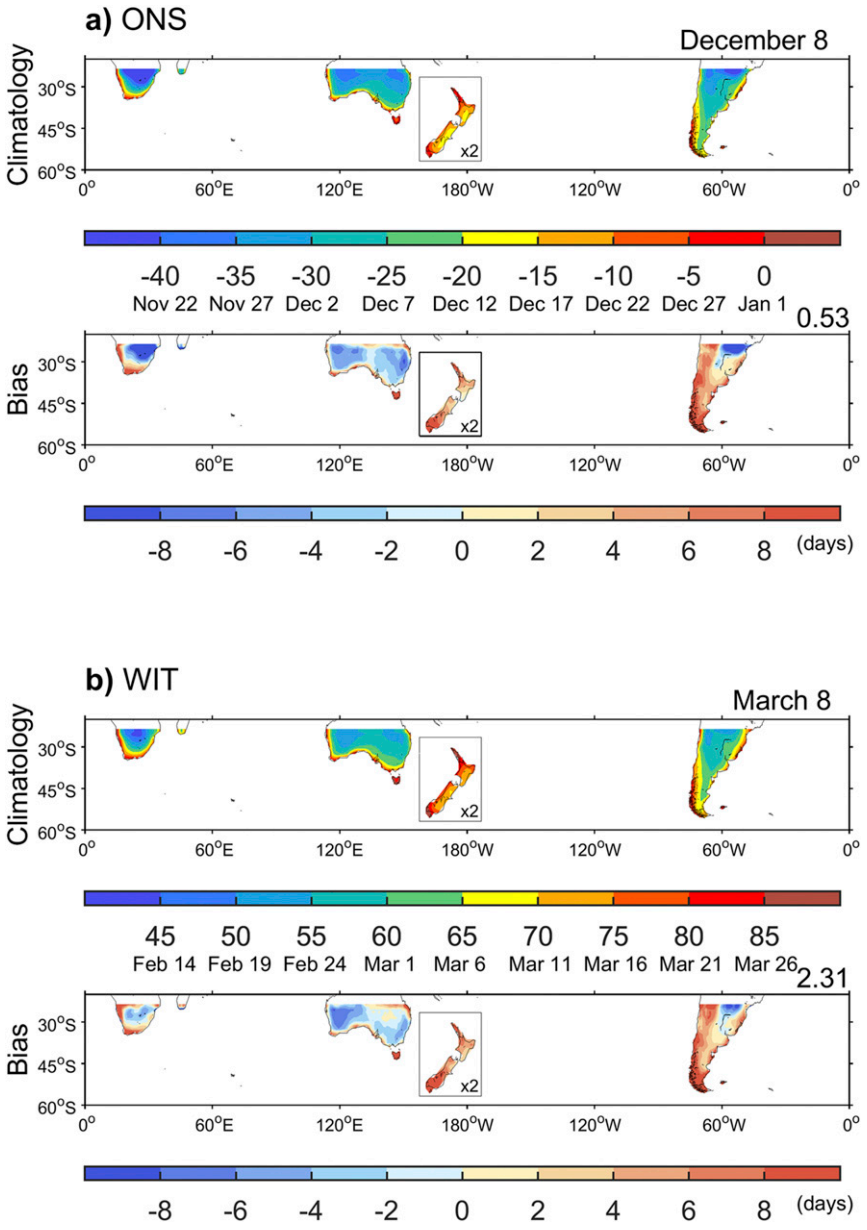

FIG. 6. CMIP5 multimodel mean spatial patterns of the climatology and bias (ALL minus observations) for (a) summer onset and (b) summer withdrawal. Area means are given in the top-right corner of each half panel.

coastal-inland contrast was weaker in models (Park et al. 2018). This is presumably due to the smaller land regions in the SH; therefore, model grid spacing is larger relative to the total land size, as evidenced by the overly strong influence of this oceanic mechanism in New Zealand. Therefore, biases in both summer-season onset and withdrawal are positive (i.e., more delayed) at the coasts and negative (i.e., earlier) farther inland (bottom rows of Figs. 6a,b). This overall bias in the SH was consistent when using a different observational dataset (i.e., HadGHCND), yet resulted in similar summer-season durations as in the observations of ~90 days (not shown).

To attribute the anthropogenic and natural contributions to the trends in the observed summer-season indices, we next construct multimodel mean trend patterns of the summer onset and withdrawal from the ALL, GHG, and NAT simulations, and are compared with the observations (Fig. 7). In the different forcing simulation maps, regions where there is less than 80% intermodel agreement in the sign of trends are hatched, and the area mean trends are provided in the top-right corners. The ALL and GHG forcing simulations show broad spatial agreement to the observations and among models for both onset and withdrawal, except for regions where the trends are

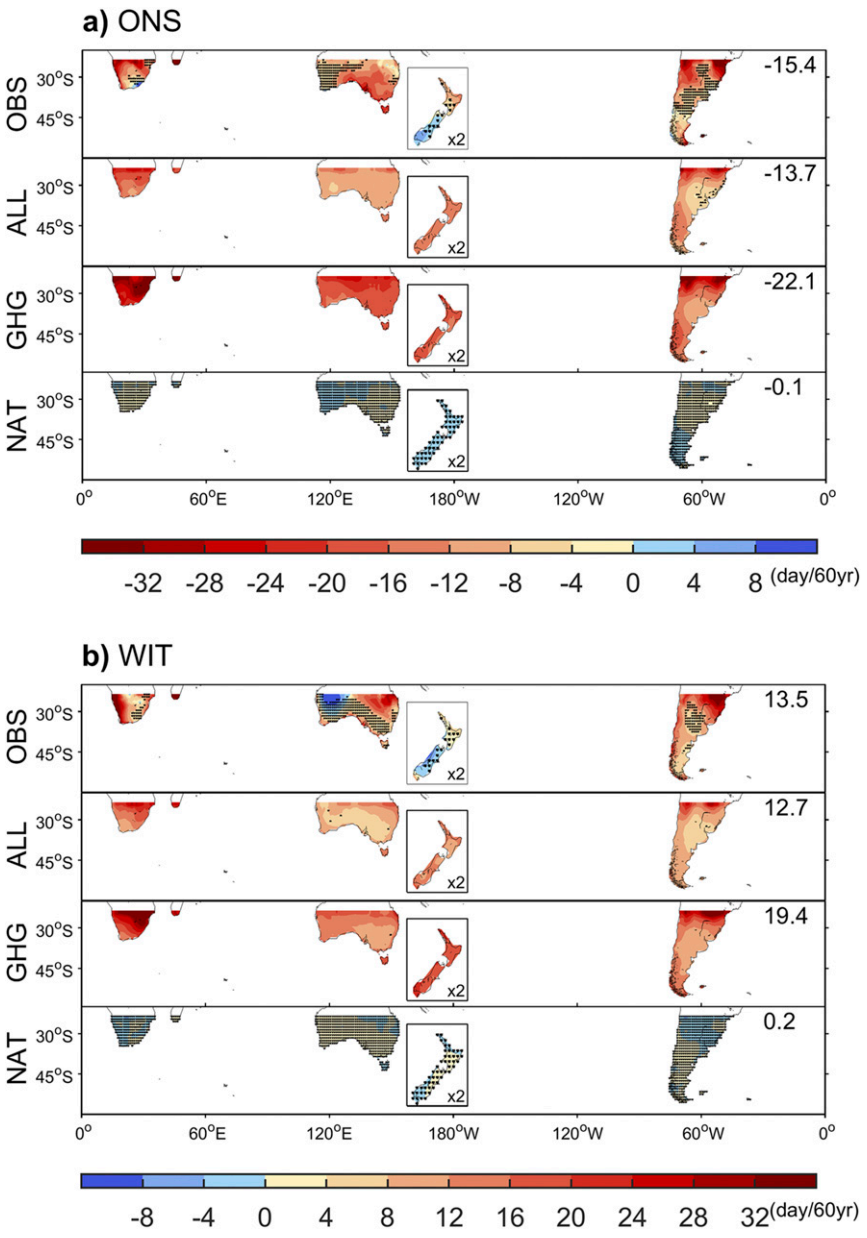

FIG. 7. CMIP5 multimodel mean spatial patterns of trends in (a) summer onset and (b) summer withdrawal for the ALL, GHG, and NAT experiments. The observed trends (OBS) with hatching the same as in Fig. 3 are provided at the top of each panel for comparison. Hatching for the CMIP5 experiments indicates grids where there is less than 80% intermodel agreement in the sign of trends. Area means are given in the top-right corner of each quarter panel.

mostly not significant in the observations (i.e., Western Australia and southern New Zealand). Trends in ALL overall are slightly weaker (by about 2 days) and much stronger (by about 6 days) in GHG relative to the observations where they are significant. Therefore, anthropogenic forcing due to the GHG increases likely played a critical role in the SH summer expansion. However, minimal change in the summer-season indices is simulated in NAT, and there is no intermodel consensus, suggesting natural (solar plus volcanic activities) forcing alone cannot explain any of the observed trends in summer-season lengthening in the SH during the 60-yr period.

Here, we assess whether the minimal asymmetry observed in the SH summer-season lengthening is simulated by the models by comparing the sum of the trends in summer onset and withdrawal from the observed and simulated spatial patterns (Fig. 8). Negative values indicate regions where the trends of change in summer onset are greater than those of withdrawal, and positive values indicate the reverse. Based on the overall

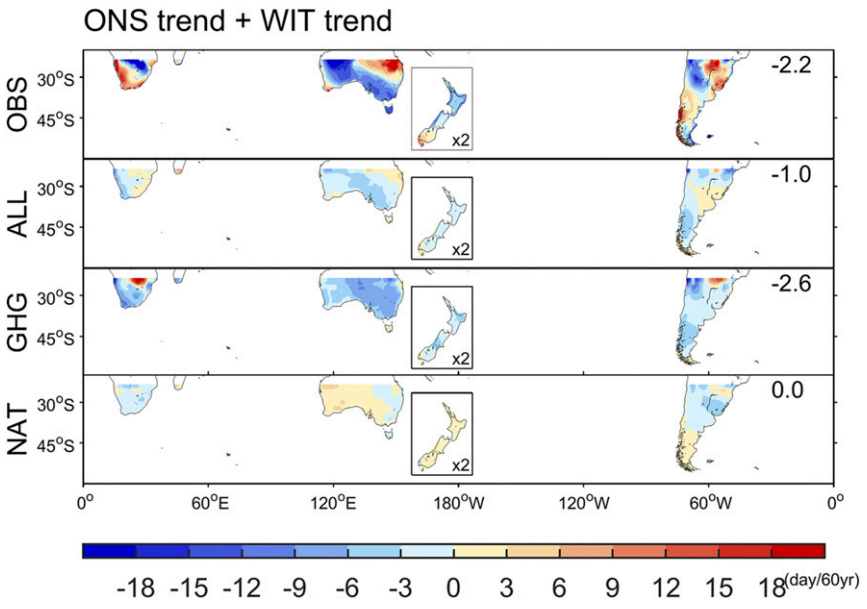

FIG. 8. Spatial patterns of the sum of trends in summer onset and withdrawal for the OBS and CMIP5 multimodel means (ALL, GHG, and NAT experiments). Area means are given in the top-right corner of each quarter panel.

observed trends of summer-season indices averaged in the SH (top row of Fig. 8), earlier summer onset contributed only slightly more to the summer duration extension than later summer withdrawal, with an area mean of −2.2 days. However, there are some regions across each landmass that do show larger contributions from delayed summer withdrawal to the summer duration extension. Observations show that earlier onset is stronger than delayed withdrawal in western regions of Australia, with a stronger delayed response than earlier onset to the northeast. This pattern is also captured by the ALL forcing simulations remarkably well, yet with reduced magnitude. More so, the ALL forcing simulations are found overall to have earlier summer onset contribute slightly more to the summer duration extension than later summer withdrawal on average, with an area mean of −1.0 days over the whole SH. The GHG forcing simulations have an area mean (−2.6 days) that is more comparable to the observations, yet the spatial patterns are inconsistent, and often of opposite sign. Interestingly, the NAT forcing simulations do not exhibit asymmetric behavior at all, suggesting that anthropogenic forcing may be responsible for the earlier summer onset contributing more to the summer duration extension than a later summer withdrawal.

To better understand some of the regional features in the observations that the models do not capture when including both anthropogenic and natural forcings (the ALL simulations), we here also consider possible large-scale influence from factors such as multidecadal variability associated with the IPO and SAM that occurs over the SH. The IPO is a large-scale, long-period oscillation that influences climate variability over the Pacific basin, and therefore may have an influence on the trends obtained over southern America, New Zealand, and Australia. Over the 60-yr period analyzed (i.e., 1953–2012), a positive trend in the IPO has occurred, transitioning from a negative phase in the earlier period (e.g., 1950s to late 1970s) to a general positive phase in the later period. Similarly, the SAM has tended toward more positive values over the same period (and linked to external forcing) and may have an influence on the trends over the southern portions of all SH landmasses. Figure 9 shows a comparison of the domain-averaged trends in summer-season indices from the observations (black bars) with those from ALL (green bars), GHG (red bars), and NAT (blue bars) simulations in order to assess which regional trends may be more attributable to external forcing or internal long-term variability such as the IPO. In addition to the multimodel averaged trends, the multimodel 5%–95% range is also shown using error bars to assess consistency with the observations. Overall, the observed trends in all three summer-season indices display the same relationship with the ALL forcing at the regional scale. For example, ALL forcing simulations slightly underestimate the trends for the entire SH, southern Africa, and southern America, reproduce the regional trend in Australia, and overestimate the trend in New Zealand. Apart from WIT for New Zealand, for all regions across the three summer-season indices, the observed trends all fall within the multimodel 5%–95% range, of which all ranges are positive. Note the ALL forced ONS trends in New Zealand range from 0 to 23 days, indicating large intermodel uncertainty. The ALL simulations overall capture the larger increase in the southern Africa and southern America domains relative to elsewhere. The GHG simulations also display this feature of the regional-scale differences, being larger in southern Africa and southern America, compared to elsewhere. Interestingly, the majority of the observed trends

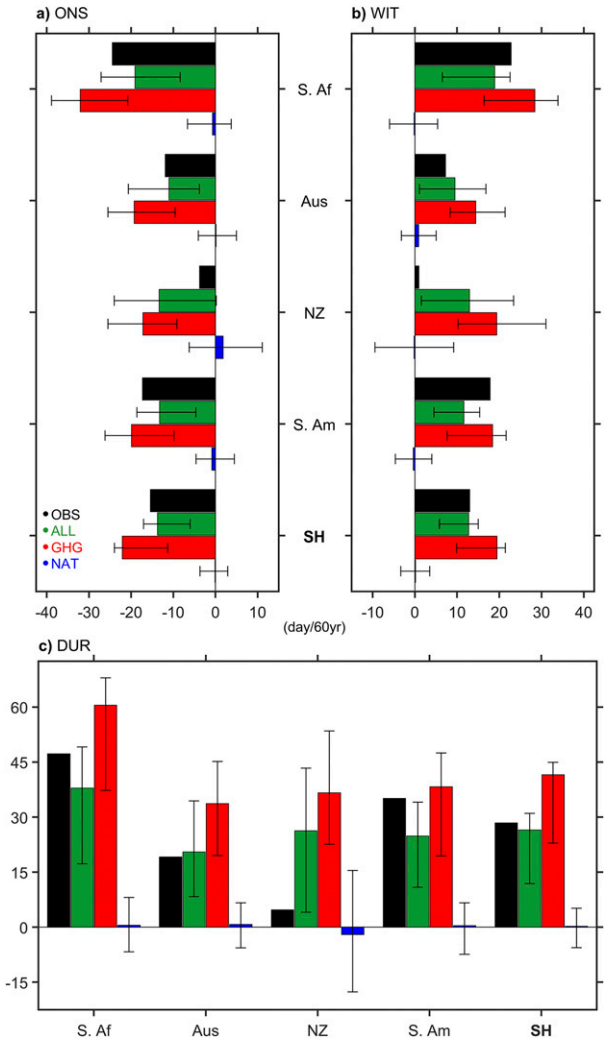

FIG. 9. Regional domain-averaged trends in (a) summer onset, (b) summer withdrawal, and (c) summer duration from OBS (black), and multimodel means for the ALL (green), GHG (red), and NAT (blue) experiments. Error bars represent the 5%–95% percentile ranges estimated using all individual runs for each experiment.

fall within the GHG multimodel 5%–95% ranges, except too-strong trends for the Australia and New Zealand domains. This latter feature in these two regions suggests that they could be influenced from aerosol cooling influences, as well as large-scale variability in the Pacific basin, such as the IPO, as it one of the dominant modes of multidecadal climate variability on both sides of the Pacific basin. For example, it is known to exert significant modulating effects on the impacts due to the ENSO on both Australia and New Zealand (e.g., Power et al. 1999; Salinger et al. 2001), and also suggested to have large contributions to accelerated warming periods over the twentieth century (Meehl et al. 2016). Last, trends from the NAT simulations fail to explain the observed changes. Only by taking into account the multimodel 5%–95% ranges do the observed trends fall within those of the NAT trends for New Zealand, yet the range crosses the zero line, deeming this unreliable. Therefore, this suggests that the long-term lengthening in the SH summer season, including both earlier onset and delayed withdrawal, is predominantly due to anthropogenic forcing associated with increasing greenhouse gases with insignificant impact of natural forcing associated with solar and volcanic activities. To test the sensitivity of the model trends to intermodel differences in climate sensitivity, we repeated the analysis using only the six models that had all simulations of ALL, GHG, and NAT forcing experiments (Fig. S2 in the online supplemental material) and found the difference to be negligible.

c. *Quantitative attribution of forced and internal contributions*

As detailed in section 2c of the methods, we also quantitatively attribute the observed trends in summer-season indices over the SH and its subregions in terms of the proportions associated with external forcing (i.e., anthropogenic plus natural) and with internal long-term variability (Fig. 10). For the whole SH, the proportion of the trend for all three summer-season indices attributable to external forcing (ALL green bars) was slightly less than 1 (a range of 0.88–0.93 across the three indices), therefore, explaining the majority of the observed trends in the SH. Similarly, at the regional scales, the proportions of trends explained by ALL forcing were generally less than 1, and in all cases, 5%–95% confidence intervals estimated from individual ALL runs (see section 2c) include the contribution of ALL forcing to the observed trend. Therefore, most of the observed trends could be robustly explained by external (anthropogenic plus natural) forcing at both the hemisphere and regional scale. The exception is New Zealand, where the proportion of the summer onset trend explained by ALL was larger, and smaller for summer withdrawal. In addition, the 5%–95% confidence interval for New Zealand summer withdrawal includes zero, representing large uncertainty due to the weak observed trend. Therefore, there may be a modest contribution of internal variability to the residual trends in this region. In addition, in some cases relatively large intermodel uncertainties in the proportion of trends attributable to external forcings were found at the regional scale, such as the southern Africa where 5%–95% confidence intervals for WIT were ~0.7, ranging from 0.71 to 1.44.

Indeed, contributions from the IPO and SAM influence were found at the regional scales (orange and yellow bars in Fig. 10, respectively). The strongest IPO influences were found over Australia and New Zealand, with weak IPO influence found over southern Africa, southern America, and less so at the hemisphere scale. The individual proportion of the trends attributable to the IPO ranged from −0.1 to +0.3 for the Australia and New Zealand regions helping to explain the larger uncertainty in the ALL forcing contribution. Overall, the largest contribution from IPO variability was to summer onset in New Zealand of about +12%. Similarly, the contribution of the IPO to withdrawal and duration in New Zealand was +8% and +9%, respectively, and all three residual portions in the summer-season indices representing positive contributions of the IPO to the observed trends in the summer-season

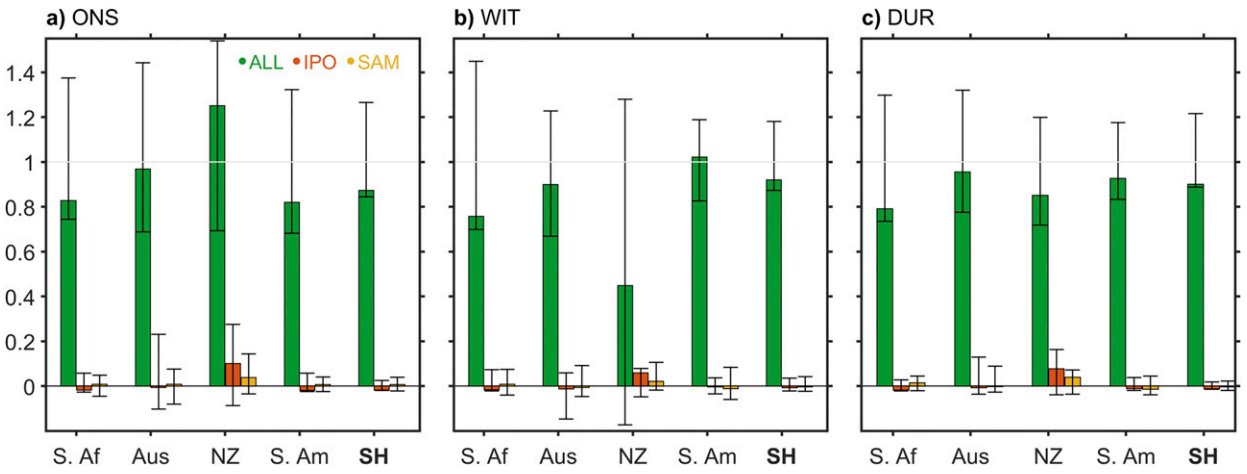

FIG. 10. Attributable trend ratios to the observed total trends of ALL forcing (green bars), IPO (orange bars), and SAM (yellow bars) for (a) summer onset, (b) summer withdrawal, and (c) summer duration. Error bars represent the 5%–95% percentile ranges of the attributable trend ratios estimated from individual models.

lengthening. The SAM influences were generally much smaller than that for the IPO, yet individual proportions of the trends attributable to the SAM ranged from −0.1 to +0.16 dependent on summer-season index. Overall, the largest contribution from SAM variability was to summer onset and duration in New Zealand of about +5%.

4. Summary and conclusions

Increasing risk of conditions associated with widespread excessive heating events observed during recent decades (Coumou and Rahmstorf 2012; Willett and Sherwood 2012; Cowan et al. 2014; Zscheischler and Seneviratne 2017; Pfleiderer et al. 2019) is only projected to increase further in the future (Meehl and Tebaldi 2004; Coumou and Robinson 2013; Argüeso et al. 2016; Tebaldi and Wehner 2018). For example, extreme heat waves are becoming more frequent and intense in many major cities worldwide (e.g., Coumou et al. 2013; Mora et al. 2017), and there has been an increase in catastrophic wildfire events (IPCC 2013; Jolly et al. 2015; Abatzoglou et al. 2019). Such events are generally tied to the ''meteorological'' summer season (e.g., Min et al. 2019).

Over the 60-yr period during 1953–2012, statistically significant lengthening of the SH summer season was identified across the majority of land regions. Overall, on average the SH summer season was found to have increased by nearly one month. However, the summer onset advance contributed only marginally (i.e., 54%–57%) more than a summer withdrawal delay to the observed increase in summer-season length in many regions. This is slightly less than that found for the NH, where the summer onset advance was found to contribute 54%–60% to the increase in the summer-season lengthening. Concerning the SH subregion trends, southern Africa displayed the strongest domain-averaged summer onset trends, yet parts of southeastern Australia and northern South America also exhibited strong trends toward earlier summer onset. Similarly, the strongest domain-averaged summer withdrawal trends were over southern Africa, and strong trends toward delayed withdrawal are also exhibited in northern South America. However, in Australia the strongest delayed withdrawal responses were observed in the northeast and significant earlier summer withdrawals over the northwest (Fig. 3b). The stronger trends of summer lengthening were consequently found more in southwestern Africa, central-to-eastern Australia, and southwestern to northern South America (Fig. 3c). Interestingly, the regions of central-to-eastern Australia and the Amazon have recently experienced extreme prolonged drought conditions and catastrophic wildfire events (Dowdy 2018). However, some caution is needed in areas with limited observational coverage.

In general, the ALL and GHG simulations were consistent with the observed trend patterns of global and regional lengthening of the summer season, except over southern New Zealand (Fig. 7). Contributions due to natural-only [solar and volcanic activities (NAT)] simulations were not significant. Therefore, the observed long-term changes in the summer-season timing and lengthening are consistent with changes associated with anthropogenic forcing caused primarily by increased greenhouse gas emissions over the SH and its subregions. Overall, the ALL simulations had a slight underestimation of the observed trends in both summer onset and withdrawal, with strong intermodel agreement (Figs. 7 and 9). In addition, both the ALL and GHG forcing simulations were found to have earlier summer onset contribute slightly more on average to the summer duration extension than later summer withdrawal. This asymmetric behavior in the models is stronger in the SH than that for the NH, yet the asymmetry in observations was found to be slightly weaker in the SH.

Contrasting regional trends in the summer-season timing and length were found over the two islands of New Zealand. Domain-averaged trends for the individual islands found the North Island exhibited a significant tendency toward a lengthening of the summer season [17.5 days $(60\,\mathrm{yr})^{-1}$; p value = 0.0447], mainly a result of earlier summer onset, and significant long-term temperature change during summer

[0.66°C $(60\,\text{yr})^{-1}$; p value = 0.0238]. Whereas the South Island exhibited a tendency toward a shorter summer season [−2.3 days $(60\,\text{yr})^{-1}$; p value > 0.1] and a long-term temperature change [0.06°C $(60\,\text{yr})^{-1}$; p value > 0.1], which are seemingly contributed to by both a delayed onset and earlier withdrawal on the summer season. This is presumably due to the vastly different mean climates and topography of the two islands, differing influence due to internal variability, and the different summer mean temperature changes over the past 60 years where only the North Island has exhibited a significant summer warming (Fig. 5a).

Consistent differences between observed and ALL simulations in regions surrounding the Pacific basin suggest that they could be influenced from forcing other than external, such large-scale internal variability. Overall, the ALL forcing explains the majority of the observed lengthening trend of the summer season over the SH, and the 5%–95% confidence intervals (which were estimated from individual model runs) include the observed trends, indicating the robustness of the external contribution to the long-term changes. In addition, the IPO and SAM contribute only a small amount to the observed trends, up to ~12% and ~5%, respectively, depending on the regions and summer-season indices. The contribution of the IPO and SAM was largest for New Zealand, where observations and ALL forcing trends showed the least agreement, and observed long-term changes are smallest. Causes of the observation–model inconsistency could be further explored using downscaling simulations due to the small landmasses, and often poorly resolved topography by the models. Further, regions that exhibit an earlier end to summer and/or shortening of the summer season (e.g., southern New Zealand and Western Australia) require further investigation, potentially with observations of higher spatial resolution or individual weather stations.

Acknowledgments. This study was supported by University of Auckland Faculty Research Development Fund (Grant 3719527) and by the National Research Foundation of Korea (NRF) grant funded by the Ministry of Science and ICT (Grant 2017R1A2B2008951). We acknowledge the World Climate Research Programme's Working Group on Coupled Modelling, which is responsible for CMIP, and we thank the climate modeling groups (listed in Table 1 of this paper) for producing and making available their model output. The authors thank the anonymous reviewers for their constructive comments on the paper.

Data availability statement. The Berkeley Earth project dataset can be obtained online (http://berkeleyearth.org/data/), and the CMIP5 dataset can be obtained through the ESGF data portals (see https://esgf-node.llnl.gov/projects/cmip5/). The IPO index was obtained from the NOAA Earth System Research Laboratory site (https://www.esrl.noaa.gov/psd/data/timeseries/IPOTPI). The SAM index was obtained from The KNMI Climate Explorer site (http://climexp.knmi.nl).

REFERENCES

Abatzoglou, J. T., A. P. Williams, and R. Barbero, 2019: Global emergence of anthropogenic climate change in fire weather indices. *Geophys. Res. Lett.*, **46**, 326–336, https://doi.org/10.1029/2018GL080959.

AghaKouchak, A., L. Cheng, O. Mazdiyasni, and A. Farahmand, 2014: Global warming and changes in risk of concurrent climate extremes: Insights from the 2014 California drought. *Geophys. Res. Lett.*, **41**, 8847–8852, https://doi.org/10.1002/2014GL062308.

Allen, M. R., and P. A. Stott, 2003: Estimating signal amplitudes in optimal fingerprinting, part I: Theory. *Climate Dyn.*, **21**, 477–491, https://doi.org/10.1007/S00382-003-0313-9.

Arblaster, J. M., and G. A. Meehl, 2006: Contributions of external forcings to southern annular mode trends. *J. Climate*, **19**, 2896–2905, https://doi.org/10.1175/JCLI3774.1.

Argüeso, D., A. Di Luca, S. Perkins-Kirkpatrick, and J. P. Evans, 2016: Seasonal mean temperature changes control future heat waves. *Geophys. Res. Lett.*, **43**, 7653–7660, https://doi.org/10.1002/2016GL069408.

Bertram, D. F., D. L. Mackas, and S. M. McKinnell, 2001: The seasonal cycle revisited: Interannual variation and ecosystem consequences. *Prog. Oceanogr.*, **49**, 283–307, https://doi.org/10.1016/S0079-6611(01)00027-1.

Caesar, J., L. Alexander, and R. Vose, 2006: Large-scale changes in observed daily maximum and minimum temperatures: Creation and analysis of a new gridded data set. *J. Geophys. Res.*, **111**, D05101, https://doi.org/10.1029/2005JD006280.

Christidis, N., P. A. Stott, S. Brown, D. J. Karoly, and J. Caesar, 2007: Human contribution to the lengthening of the growing season during 1950–99. *J. Climate*, **20**, 5441–5454, https://doi.org/10.1175/2007JCLI1568.1.

Clem, K. R., and Coauthors, 2020: Record warming at the South Pole during the past three decades. *Nat. Climate Change*, **10**, 762–770, https://doi.org/10.1038/s41558-020-0815-z.

Cornes, R., P. Jones, and C. Qian, 2017: Twentieth-century trends in the annual cycle of temperature across the Northern Hemisphere. *J. Climate*, **30**, 5755–5773, https://doi.org/10.1175/JCLI-D-16-0315.1.

Coumou, D., and S. Rahmstorf, 2012: A decade of weather extremes. *Nat. Climate Change*, **2**, 491–496, https://doi.org/10.1038/NCLIMATE1452.

——, and A. Robinson, 2013: Historic and future increase in the global land area affected by monthly heat extremes. *Environ. Res. Lett.*, **8**, 034018, https://doi.org/10.1088/1748-9326/8/3/034018.

——, ——, and S. Rahmstorf, 2013: Global increase in record-breaking monthly-mean temperatures. *Climatic Change*, **118**, 771–782, https://doi.org/10.1007/S10584-012-0668-1.

Cowan, T., A. Purich, S. Perkins, A. Pezza, G. Boschat, and K. Sadler, 2014: More frequent, longer, and hotter heat waves for Australia in the twenty-first century. *J. Climate*, **27**, 5851–5871, https://doi.org/10.1175/JCLI-D-14-00092.1.

Dowdy, A. J., 2018: Climatological variability of fire weather in Australia. *J. Appl. Meteor. Climatol.*, **57**, 221–234, https://doi.org/10.1175/JAMC-D-17-0167.1.

Dwyer, J. G., M. Biasutti, and A. H. Sobel, 2012: Projected changes in the seasonal cycle of surface temperature. *J. Climate*, **25**, 6359–6374, https://doi.org/10.1175/JCLI-D-11-00741.1.

Gerber, E. P., and S.-W. Son, 2014: Quantifying the summertime response of the austral jet stream and Hadley cell to stratospheric ozone and greenhouse gases. *J. Climate*, **27**, 5538–5559, https://doi.org/10.1175/JCLI-D-13-00539.1.

Gillett, N. P., and J. C. Fyfe, 2013: Annular mode changes in the CMIP5 simulations. *Geophys. Res. Lett.*, **40**, 1189–1193, https://doi.org/10.1002/GRL.50249.

Gong, D., and S. Wang, 1999: Definition of Antarctic Oscillation index. *Geophys. Res. Lett.*, **26**, 459–462, https://doi.org/10.1029/1999GL900003.

Hao, Z., A. AghaKouchak, and T. J. Phillips, 2013: Changes in concurrent monthly precipitation and temperature extremes.

Environ. Res. Lett., **8**, 034014, https://doi.org/10.1088/1748-9326/8/3/034014.

Harris, S., and C. Lucas, 2019: Understanding the variability of Australian fire weather between 1973 and 2017. *PLOS ONE*, **14**, e0222328, https://doi.org/10.1371/journal.pone.0222328.

Hendon, H. H., D. W. J. Thompson, and M. C. Wheeler, 2007: Australian rainfall and surface temperature variations associated with the Southern Hemisphere annular mode. *J. Climate*, **20**, 2452–2467, https://doi.org/10.1175/JCLI4134.1.

Henley, B. J., J. Gergis, D. J. Karoly, S. B. Power, J. Kennedy, and C. K. Folland, 2015: A tripole index for the interdecadal Pacific oscillation. *Climate Dyn.*, **45**, 3077–3090, https://doi.org/10.1007/s00382-015-2525-1.

——, and Coauthors, 2017: Spatial and temporal agreement in climate model simulations of the interdecadal Pacific oscillation. *Environ. Res. Lett.*, **12**, 044011, https://doi.org/10.1088/1748-9326/aa5cc8.

IPCC, 2013: *Climate Change 2013: The Physical Science Basis*. Cambridge University Press, 1535 pp., https://doi.org/10.1017/CBO9781107415324.

Jolly, W. M., M. A. Cochrane, P. H. Freeborn, Z. A. Holden, T. J. Brown, G. J. Williamson, and D. M. J. S. Bowman, 2015: Climate-induced variations in global wildfire danger from 1979 to 2013. *Nat. Comms.*, **6**, 7537, https://doi.org/10.1038/ncomms8537.

Klein Tank, A. M. G., and G. P. Können, 2003: Trends in indices of daily temperature and precipitation extremes in Europe, 1946–99. *J. Climate*, **16**, 3665–3680, https://doi.org/10.1175/1520-0442(2003)016<3665:TIIODT>2.0.CO;2.

Kong, Q., S. B. Guerreiro, S. Blenkinsop, Z.-F. Li, and H. J. Fowler, 2020: Increases in summertime concurrent drought and heatwave in eastern China. *Wea. Climate Extreme*, **28**, 100242, https://doi.org/10.1016/j.wace.2019.100242.

Lehmann, J., F. Mempel, and D. Coumou, 2018: Increased occurrence of record-wet and record-dry months reflect changes in mean rainfall. *Geophys. Res. Lett.*, **45**, 13 468–13 476, https://doi.org/10.1029/2018GL079439.

Mann, M. E., and J. Park, 1996: Greenhouse warming and changes in the seasonal cycle of temperature: Model versus observations. *Geophys. Res. Lett.*, **23**, 1111–1114, https://doi.org/10.1029/96GL01066.

Meehl, G. A., and C. Tebaldi, 2004: More intense, more frequent, and longer lasting heat waves in the 21st century. *Science*, **305**, 994–997, https://doi.org/10.1126/science.1098704.

——, J. M. Arblaster, and G. Branstator, 2012: Mechanisms contributing to the warming hole and the consequent U.S. east–west differential of heat extremes. *J. Climate*, **25**, 6394–6408, https://doi.org/10.1175/JCLI-D-11-00655.1.

——, A. Hu, B. D. Santer, and S.-P. Xie, 2016: Contribution of the interdecadal Pacific oscillation to twentieth-century global surface temperature trends. *Nat. Climate Change*, **6**, 1005–1008, https://doi.org/10.1038/nclimate3107.

Min, S.-K., W. Cai, and P. Whetton, 2013: Influence of climate variability on seasonal extremes over Australia. *J. Geophys. Res. Atmos.*, **118**, 643–654, https://doi.org/10.1002/jgrd.50164.

——, Y.-H. Kim, I.-H. Park, D. Lee, S. Sparrow, D. Wallom, and D. Stone, 2019: Anthropogenic contribution to the 2017 earliest summer onset in South Korea. *Bull. Amer. Meteor. Soc.*, **100**, S73–S77, https://doi.org/10.1175/BAMS-D-18-0096.1.

Mora, C., and Coauthors, 2017: Global risk of deadly heat. *Nat. Climate Change*, **7**, 501–506, https://doi.org/10.1038/nclimate3322.

Mueller, B., M. Hauser, C. Iles, R. H. Rimi, F. W. Zwiers, and H. Wan, 2015: Lengthening of the growing season in wheat and maize producing regions. *Wea. Climate Extreme*, **9**, 47–56, https://doi.org/10.1016/j.wace.2015.04.001.

Paik, S., S.-K. Min, Y.-H. Kim, B.-M. Kim, H. Shiogama, and J. Heo, 2017: Attributing causes of 2015 record minimum sea-ice extent in the Sea of Okhotsk. *J. Climate*, **30**, 4693–4703, https://doi.org/10.1175/JCLI-D-16-0587.1.

Park, B.-J., Y.-H. Kim, S.-K. Min, and E.-P. Lim, 2018: Anthropogenic and natural contributions to the lengthening of the summer season in the Northern Hemisphere. *J. Climate*, **31**, 6803–6819, https://doi.org/10.1175/JCLI-D-17-0643.1.

Peña-Oritz, C., D. Barriopedro, and R. Garcia-Herrera, 2015: Multidecadal variability of the summer length in Europe. *J. Climate*, **28**, 5375–5388, https://doi.org/10.1175/JCLI-D-14-00429.1.

Pfleiderer, P., C.-F. Schleussner, K. Kornhuber, and D. Coumou, 2019: Summer weather becomes more persistent in a 2°C world. *Nat. Climate Change*, **9**, 666–671, https://doi.org/10.1038/s41558-019-0555-0.

Power, S., T. Casey, C. K. Folland, A. W. Colman, and V. Mehta, 1999: Inter-decadal modulation of the impact of ENSO on Australia. *Climate Dyn.*, **15**, 319–324, https://doi.org/10.1007/s003820050284.

Qian, C., and X. Zhang, 2015: Human influences on changes in the temperature seasonality in mid- to high-latitude land areas. *J. Climate*, **28**, 5908–5921, https://doi.org/10.1175/JCLI-D-14-00821.1.

——, Z. W. Yan, and C. B. Fu, 2012: Climatic changes in the twenty-four solar terms during 1960–2008. *Chin. Sci. Bull.*, **57**, 276–286, https://doi.org/10.1007/s11434-011-4724-4.

Rohde, R., and Coauthors, 2013: A new estimate of the average Earth surface land temperature spanning 1753 to 2011. *Geoinf. Geostat. Overview*, **1**, https://doi.org/10.4172/2327-4581.1000101.

Salinger, M. J., J. A. Renwick, and A. B. Mullan, 2001: Interdecadal Pacific oscillation and South Pacific climate. *Int. J. Climatol.*, **21**, 1705–1721, https://doi.org/10.1002/joc.691.

Stine, A. R., and P. Huybers, 2012: Changes in the seasonal cycle of temperature and atmospheric circulation. *J. Climate*, **25**, 7362–7380, https://doi.org/10.1175/JCLI-D-11-00470.1.

——, ——, and I. Y. Fung, 2009: Changes in the phase of the annual cycle of surface temperature. *Nature*, **457**, 435–440, https://doi.org/10.1038/nature07675.

Swart, N. C., J. C. Fyfe, N. Gillett, and G. J. Marshall, 2015: Comparing trends in the southern annular mode and surface westerly jet. *J. Climate*, **28**, 8840–8859, https://doi.org/10.1175/JCLI-D-15-0334.1.

Taylor, K. E., R. J. Stouffer, and G. A. Meehl, 2012: An overview of CMIP5 and the experiment design. *Bull. Amer. Meteor. Soc.*, **93**, 485–498, https://doi.org/10.1175/BAMS-D-11-00094.1.

Tebaldi, C., and M. F. Wehner, 2018: Benefits of mitigation for future heat extremes under RCP4.5 compared to RCP8.5. *Climatic Change*, **146**, 349–361, https://doi.org/10.1007/s10584-016-1605-5.

Trenberth, K. E., 1983: What are the seasons? *Bull. Amer. Meteor. Soc.*, **64**, 1276–1282, https://doi.org/10.1175/1520-0477(1983)064<1276:WATS>2.0.CO;2.

Wallace, C. J., and T. J. Osborn, 2002: Recent and future modulation of the annual cycle. *Climate Res.*, **22**, 1–11, https://doi.org/10.3354/CR022001.

Willett, K. M., and S. Sherwood, 2012: Exceedance of heat index thresholds for 15 regions under a warming climate using the wet-bulb globe temperature. *Int. J. Climatol.*, **32**, 161–177, https://doi.org/10.1002/JOC.2257.

Williams, A. P., J. T. Abatzoglou, A. Gershunov, J. Guzman-Morales, D. A. Bishop, J. K. Balch, and D. P. Lettenmaier, 2019: Observed impacts of anthropogenic climate change on wildfire in California. *Earth's Future*, **7**, 892–910, https://doi.org/10.1029/2019EF001210.

Zscheischler, J., and S. I. Seneviratne, 2017: Dependence of drivers affects risks associated with compound events. *Sci. Adv.*, **3**, e1700263, https://doi.org/10.1126/SCIADV.1700263.